Supplementary Information for Charge Transport and Mobility Relaxation in Organic Bulk Heterojunction Morphologies Derived from Electron Tomography Measurements

Michael C. Heiber,[1, 2, *] Andrew A. Herzing,[3] Lee J. Richter,[2] and Dean M. DeLongchamp[2, †]

[1] *Center for Hierarchical Materials Design (CHiMaD),*
Northwestern University, Evanston, Illinois 60208, USA

[2] *Materials Science and Engineering Division, National Institute of Standards and Technology, Gaithersburg, MD 20899, USA*

[3] *Materials Measurement Science Division, National Institute of Standards and Technology, Gaithersburg, MD 20899, USA*

(Dated: June 27, 2020)

I.   ADDITIONAL MORPHOLOGY INFORMATION

In addition to the visualization and analysis of the bulk heterojunction structure from the tomography data provided in the main text, several additional characterizations were performed using the data generated by the Ising_OPV software tool. In addition to the small cross-sectional images of one extracted sub-section of the interpreted tomography data, full cross sections were also created and are shown in Fig. 1. Here, one can see that the main structural differences in domain size and hierarchical structure noted in the main text are present throughout the film.
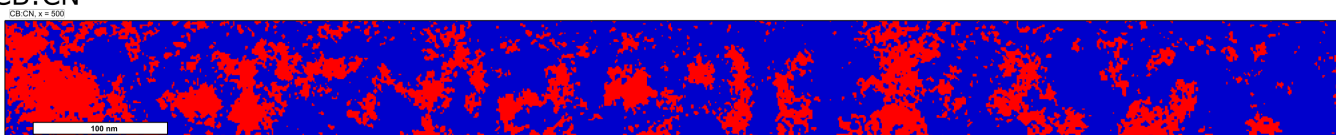
CB
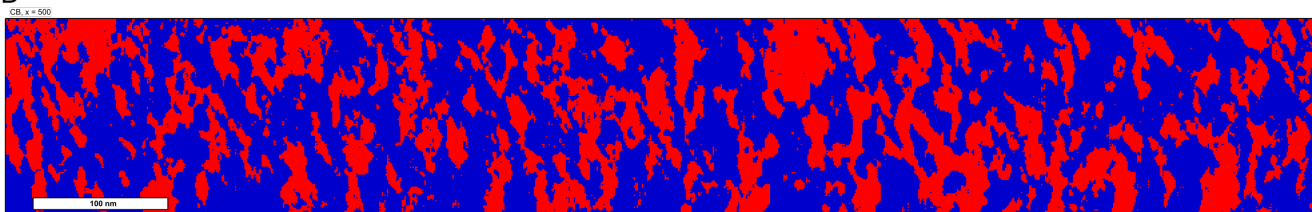
DCB
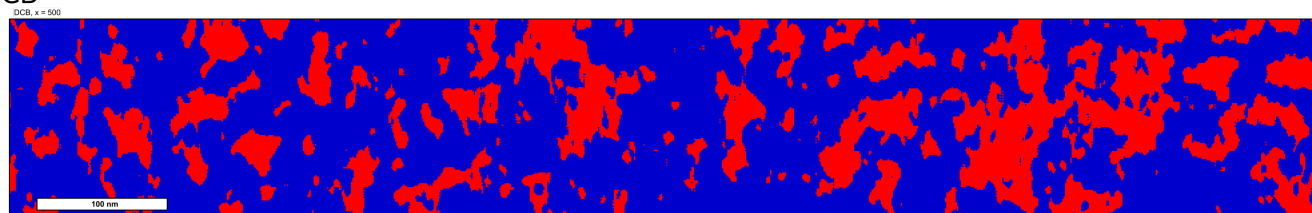
CB:CN

FIG. 1. Full cross-sectional images of the interpreted tomography data.

Beyond the features notable in cross-sectional images, Ising_OPV also provided areal data to help gauge film uniformity, defect density, or other features in the x-y plane. First, Fig. 2 shows the areal composition maps of the three interpreted tomography datasets. One sample was prepared from a chlorobenzene (CB) solvent formulation, one from a 1,2-dichlorobenzene (DCB) formulation, and the last from a chlorobenzene:1-chloronaphthalene solvent mixture with 2 vol% CN (CB:CN). These three variants will be hereafter referred to as the CB, DCB, and CB:CN samples. One can see some degree of a compositional gradient in the DCB sample. In all samples, there is clear compositional heterogeneity with large peaks in the donor volume fraction and strong valleys with high acceptor volume fraction. This is the expected consequence of a morphology where domains are elongated out of the film plane, where there are almost completely direct charge transport pathways through the entire film thickness. Another noteworthy feature is that the fiber-like structure seen in the plan view transmission electron microscopy (TEM) images does not persist through the entire thickness of the films. The compositional heterogeneity of the DCB and CB:CN films appear nodular indicating that the elongated donor fibrillar features do not persist through the majority of the film thickness. If they did, one would expect to see similar structural features in the compositional maps.
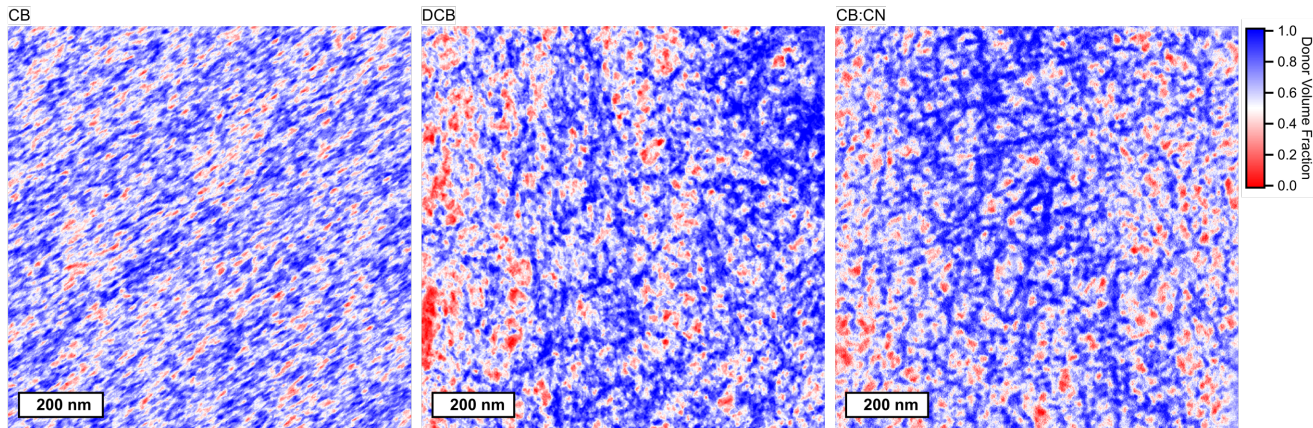

FIG. 2. Areal composition maps of the interpreted tomography data.

Another related way to look at the structure is through the tortuosity maps shown in Fig. 3. The tortuosity should be affected by compositional fluctuations, and one can gauge how uniform the tortuosity is across the film area. The donor phase tortuosity is generally low in all three samples and shows only very weak and broad tortuosity peaks, while the acceptor phase tortuosity maps have significantly more variation as discussed in the main text. Nevertheless, one can observe significant correlation between the composition maps and the donor tortuosity maps, where regions rich in donor content generally have the lowest tortuosity.
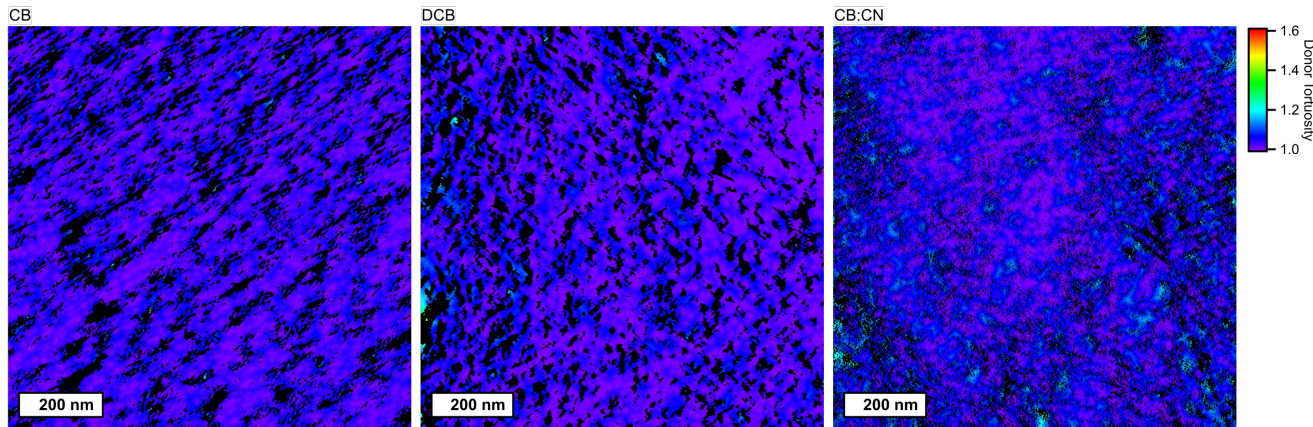

FIG. 3. Areal donor tortuosity maps of the interpreted tomography data.

Three Ising-based model morphologies were created with varying domain size and tortuosity. Following previous methods, anisotropic interactions energies were used to control the anisotropy of the domains and thereby modulate the tortuosity.[1] Table I lists the parameters used to create the morphology sets in the Ising_OPV software tool and some of their additional characteristics.[2]

TABLE I. Ising-based morphology set information. Where applicable, values are shown ± one standard deviation.

	Ising1	Ising2	Ising3
Initial lattice length/width	70	70	70
Initial lattice height	74	74	74
Initial composition	0.625	0.625	0.0635
Interaction energy, J	0.35	0.35	0.4
z-direction interaction adjustment, ΔJ_z	0.05	0.05	0
Monte Carlo steps	580	150	650
Rescale factor	2	2	2
Smoothing threshold	0.52	0.52	0.52
Final composition	0.65	0.65	0.65
Domain anisotropy, γ_d	1.68±0.05	1.29±0.03	1.05±0.05

Cross-sectional images of the the Ising-based morphology sets are shown in Fig. 4. In general, the Ising-based model produces morphologies with relatively well-defined domain sizes and smooth interfaces. In contrast, the realistic morphologies derived from the electron tomography measurements are much more irregular.
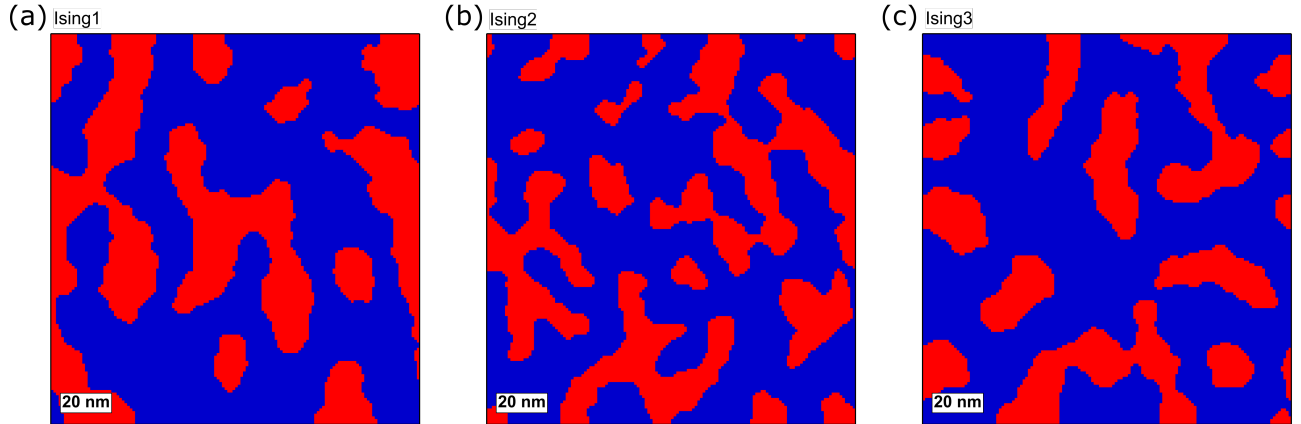

(a) Ising1 (b) Ising2 (c) Ising3

FIG. 4. Ising-based model morphology cross-sectional images.

Figure 5 shows the compositional autocorrelation data for each of the morphology sets. Data from the CB and DCB samples can be fit with single exponential functions yielding the correlation length parameter shown on the figure, but the CB:CN data needed to be fit with a double exponential function, which reflects the hierarchical nature of the morphology. Two distinct feature sizes can be extracted from the CB:CN data. In contrast, the Ising-based morphologies could not be fit well to a single exponential function since their decay is more linear.

Figure 6 shows the vertical composition and domain size profiles for each of the morphologies. All of the real morphologies showed significant enhancement of the poly(3-hexylthiophene) (P3HT) donor near the interfaces. This enrichment was particularly strong in the CB and CB:CN morphologies and could potentially explain some of the different transport phenomena observed in these morphologies. The domain size differences at the interfaces appear relatively minor in most of the morphologies, but the CB:CN morphology in particular has much smaller acceptor domains at the top surface where electrons are created during the time-of-flight simulation. This depletion of the acceptor and reduction of the domain size puts the morphology closer to the percolation limit and could potentially explain the anomalous mobility and energy relaxation dynamics.
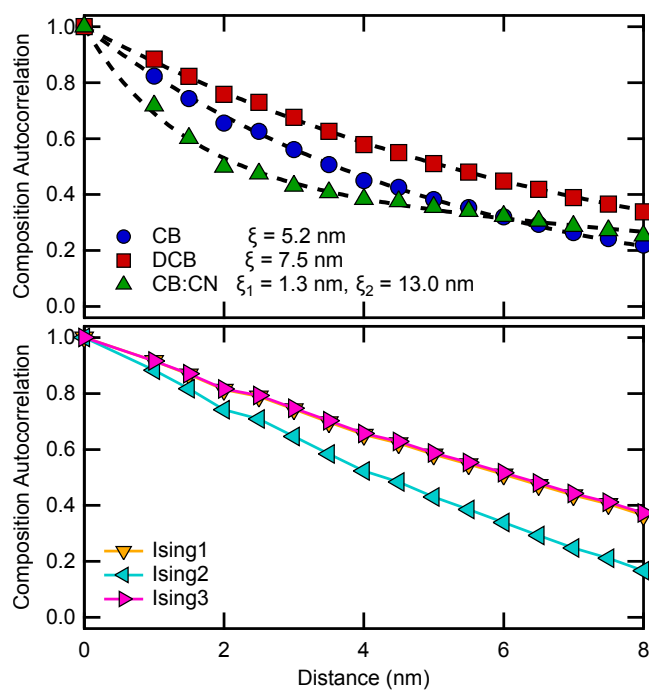
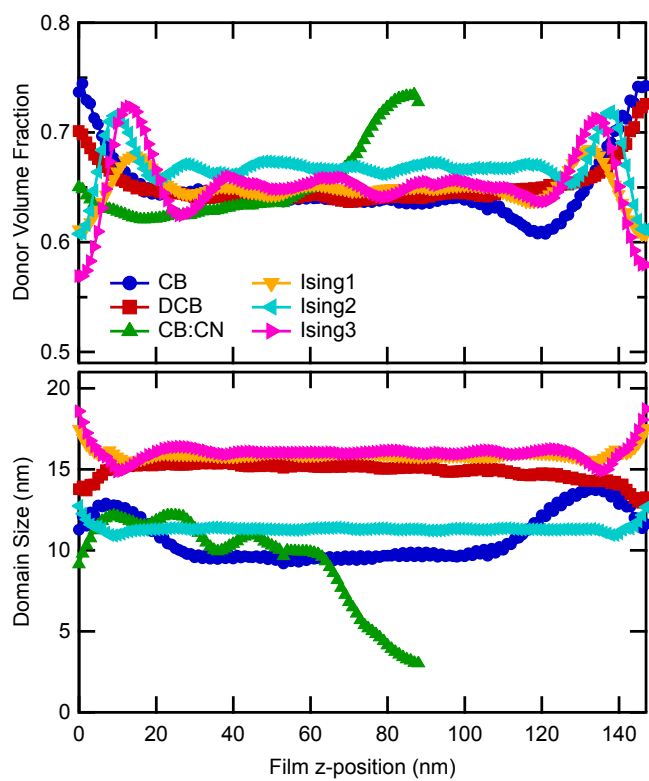FIG. 5. Compositional autocorrelation data for each morphology set.

FIG. 6. Film vertical composition and domain size data.

II.   ADDITIONAL SIMULATION INFORMATION

For the time-of-flight charge transport simulations, a thin sheet of five charge carriers were placed randomly at a surface plane of the lattice (on donor sites for holes and on acceptor sites for electrons) and then allowed to undergo charge transport through the film. For electron transport tests, the carriers were started at the top of the lattice ($z = H - 1$), and for hole transport tests, the carriers were started at the bottom on the lattice ($z = 0$). Each transient simulation was performed until reaching a cutoff time of 0.5 ms. After this cutoff time, any charge carriers still trapped in the lattice were removed, the site energies were randomly reassigned, and the process was repeated 100 times for a total of 500 charge carriers on a given morphology. Simulations were performed in parallel on 96 processors, in which each core was randomly assigned one of the morphologies from the morphology set. In total, for each time-of-flight simulation, 48,000 charge carriers were simulated on each morphology set, and the final data was obtained by averaging over the 96 independent simulations.

The majority of the parameters used for the kinetic Monte Carlo (KMC) time-of-flight charge transport simulations are provided in the main text. However, the remaining simulation parameters are listed in Table II.

TABLE II. Additional KMC parameters.

Attempt to hop frequency, ν_0	10^{12} s^{-1}
Charge localization, γ	2 nm^{-1}
Hop cutoff radius, $r_{\text{cut,hop}}$	3 nm
Dielectric constant, ϵ	3.5
Event recalculation cutoff radius, r_{recalc}	3 nm

As discussed in the main text, the equation

$$\frac{\mu_{\text{BHJ}}}{\mu_{\text{neat}}} = f\left(\hat{\sigma}, \tau\right) \exp\left[g\left(\hat{\sigma}, \tau\right) \sqrt{\frac{F}{F_0}}\right], \tag{1}$$

was used to describe the electric-field-dependent mobility data. Equation 1 describes the data very well in the low electric field regime, but the normalized mobility begins to saturate at higher electric field values and deviates from Eqn. 1. Figure 7 shows the fits of the linearized form of the equation,

$$\ln\left[\frac{\mu_{\text{BHJ}}}{\mu_{\text{neat}}}\right] = \ln\left[f\left(\hat{\sigma}, \tau\right)\right] + g\left(\hat{\sigma}, \tau\right) \sqrt{\frac{F}{F_0}}, \tag{2}$$
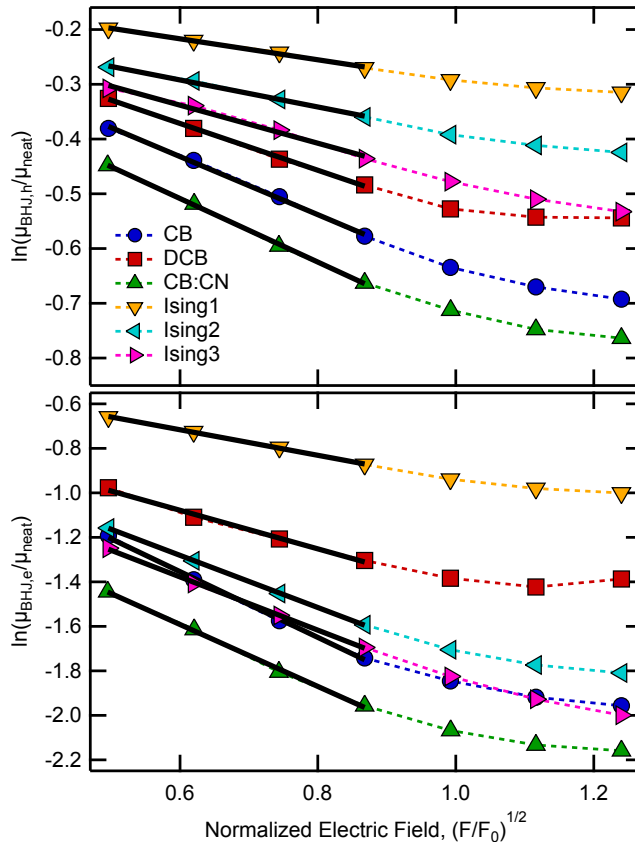
to the normalized mobility data.

FIG. 7. Solid line fits to the normalized hole mobility data (top) and electron mobility data (bottom) at low-field to extract f and g parameters.

The f and g fit parameters and their uncertainties are provided in Table III. Generally, the fit uncertainties were very low due to the high statistical sampling that was performed.

TABLE III. Electric-Field-Dependent Mobility Fitting Results showing extracted fit parameter values ± one standard deviation.

Morphology	carrier type	f	g
CB	holes	0.89 ± 0.01	-0.53 ± 0.02
DCB	holes	0.89 ± 0.007	-0.43 ± 0.01
CB:CN	holes	0.85 ± 0.006	-0.58 ± 0.01
Ising1	holes	0.92 ± 0.005	-0.19 ± 0.009
Ising2	holes	0.87 ± 0.006	-0.25 ± 0.01
Ising3	holes	0.88 ± 0.02	-0.35 ± 0.03
CB	electrons	0.63 ± 0.02	-1.48 ± 0.04
DCB	electrons	0.57 ± 0.02	-0.87 ± 0.05
CB:CN	electrons	0.47 ± 0.01	-1.39 ± 0.04
Ising1	electrons	0.69 ± 0.007	-0.57 ± 0.01
Ising2	electrons	0.56 ± 0.003	-1.17 ± 0.009
Ising3	electrons	0.52 ± 0.007	-1.20 ± 0.02

Figure 8 shows the electron transit time probability histograms for the neat material and each of the experimental bulk heterojunction (BHJ) morphologies. While the neat material produces very symmetric histograms when plotted versus $log(t)$, the BHJ morphologies are asymmetric and especially so at higher electric field values. These asymmetric histograms with a long tail is the expected behavior with dispersive transport. The neat material also yields transit time histograms that become narrower as the electric field increases, while the BHJ morphologies cause histogram broadening with increasing electric field.
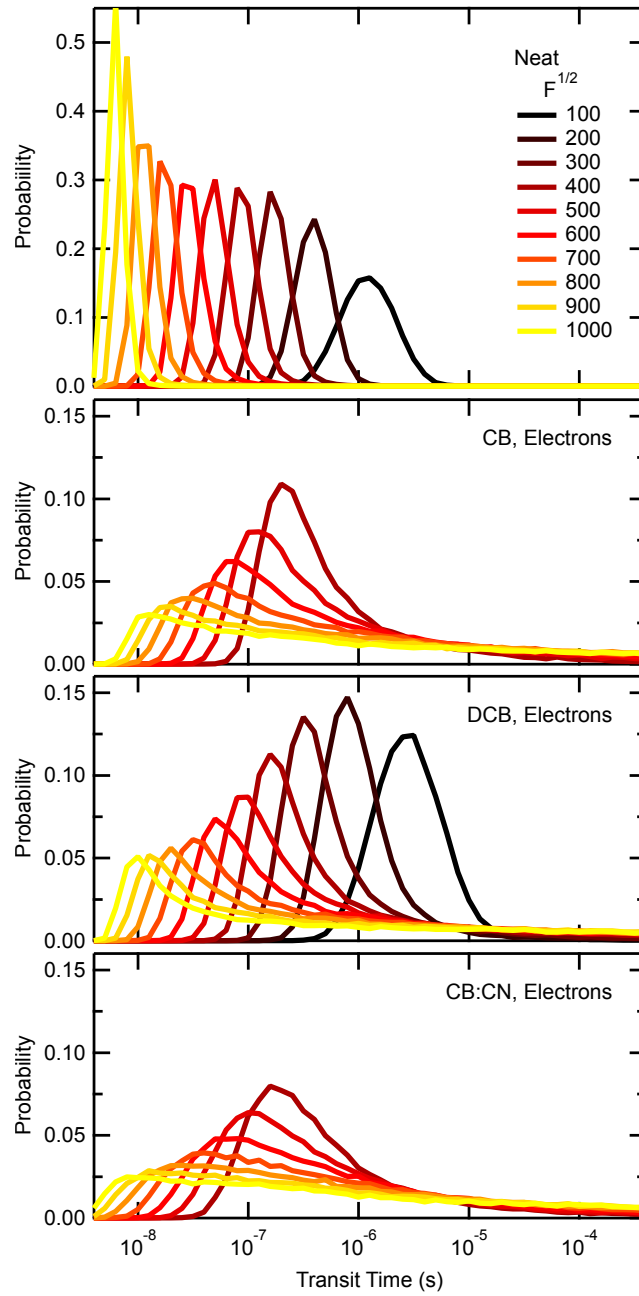
FIG. 8. Electron transit time probability histograms for each morphology set at different electric field values.

At very high electric field values, the simulation cuts off the end of transit time histogram tail. However, the cutoff time has been set to a long time of 0.5 ms so that most of charge carriers are still able to be extracted and a representative mean mobility value is able to be calculated. Simulations with a shorter cutoff time can cause an overestimated mobility at high electric field due to the fact that the carriers with a much longer transit time are then not included in the mobility calculation. As done previously,[1] the mobility is calculated using the mean of the inverse transit time,

$$\mu = \frac{L}{F} \left\langle \frac{1}{t_{\text{tr}}} \right\rangle, \tag{3}$$

where L is the lattice thickness and t_{tr} is the transit time. For accurate high electric field mobility results, it is important to use a long time-of-flight cutoff time. However, this also significantly increases the overall calculation time. The total calculation time scales roughly linearly with the the cutoff time and with the 0.5 ms cutoff time used here, calculation walltimes were about 20 hrs for each time-of-flight simulation on the real BHJ morphologies. Neat

material calculation times were more than an order of magnitude less.

Figure 9 shows the extracted mobility relaxation time (τ_{rel}) from the mobility relaxation data on the thick neat material. This was determined at the time point where the mobility reaches 10% of the steady state (long-time) value. This data further shows how strongly the transition time from dispersive to nondispersive transport in a neat material depends on the magnitude of the electric field applied.
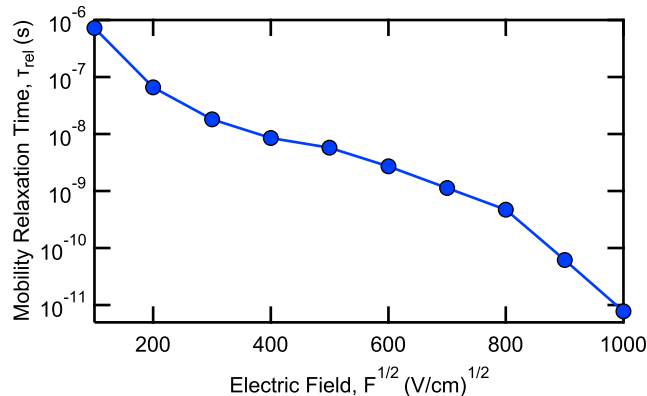

FIG. 9. Estimated mobility relaxation time from the thick neat material simulations.

Figure 10 shows the extracted equilibration energy (ϵ_∞) from the thick neat material simulations as a function of the applied electric field. Estimates for the equilibration energy were extracted from the final data point of the site occupation energy transients presented in the main text. We find that the electric-field dependence of the equilibration energy can be fit using a simple power function, where the $\epsilon_\infty \propto F^{1.4}$.
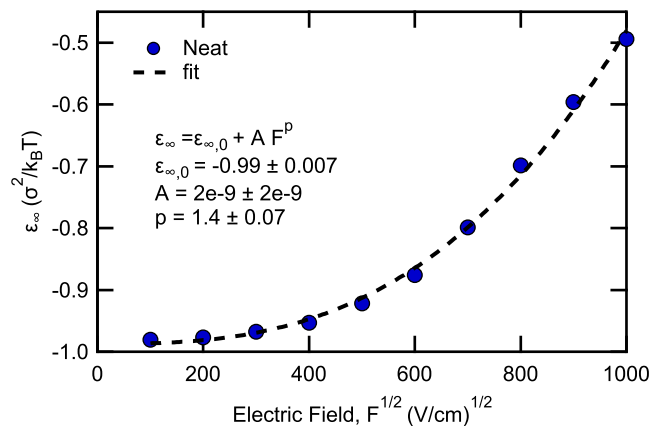

FIG. 10. Equilibration energy extracted from the thick neat material simulations.

* heiber@mailaps.org
† dean.delongchamp@nist.gov

[1] M. C. Heiber, K. Kister, A. Baumann, V. Dyakonov, C. Deibel, and T.-Q. Nguyen, Phys. Rev. Appl. **8**, 054043 (2017).
[2] M. C. Heiber, J. Open Source Software **3**, 1072 (2019).